

Spatial Profiles of NeVI-NeX Emission in ECR-Heated Discharges of the Large Helical Device with Divertor Detachment Induced by RMP Application and Ne Impurity Seeding^{*)}

Tetsutarou OISHI^{1,2)}, Masahiro KOBAYASHI^{1,2)}, Hiromi TAKAHASHI^{1,2)}, Yuki HAYASHI¹⁾, Kiyofumi MUKAI^{1,2)}, Shigeru MORITA^{1,2)}, Motoshi GOTO^{1,2)}, Yasuko KAWAMOTO¹⁾, Tomoko KAWATE^{1,2,3)}, Suguru MASUZAKI^{1,2)}, Chihiro SUZUKI^{1,2)}, Gakushi KAWAMURA^{1,2)}, Gen MOTOJIMA^{1,2)} and Ryosuke SEKI^{1,2)}

¹⁾National Institute for Fusion Science, National Institutes of Natural Sciences, 322-6 Oroshi-cho, Toki, Gifu 509-5292, Japan

²⁾Department of Fusion Science, The Graduate University for Advanced Studies, SOKENDAI, 322-6 Oroshi-cho, Toki, Gifu 509-5292, Japan

³⁾National Astronomical Observatory of Japan, 2-21-1 Osawa, Mitaka, Tokyo 181-8588, Japan

(Received 9 December 2021 / Accepted 18 February 2022)

In the Large Helical Device, the divertor detachment has been attempted by application of resonant magnetic perturbation (RMP) field and Ne gas puffing in electron cyclotron resonance- heated discharges for compatibility of high central electron temperature and low divertor heat load. Two kinds of divertor detachment phases were observed. The first one appeared transiently just after the Ne gas puffing (1st detachment), and the second one appeared steadily in the latter half of the discharge (2nd detachment). Space-resolved extreme ultraviolet spectroscopy revealed that NeVI-NeVIII emissions increased slightly outside the last closed flux surface (LCFS), while NeIX and NeX emissions increased inside the LCFS in the 1st detachment phase. Although in the 1st detachment the divertor heat load was significantly reduced, the central electron temperature also decreased because the Ne ions were penetrated inside the LCFS as a radiation source. In the 2nd detachment phase, NeVI-NeVIII emissions increased outside the LCFS while NeIX and NeX emissions kept low intensity inside the LCFS. In this phase, low divertor heat load and high central electron temperature were obtained simultaneously because the Ne ions were localized outside the LCFS as a radiation source. The profile measurements of Ne emission show that the edge island structure created by the RMP application impacts on the impurity emission distribution, where the peak of the emission shifts radially stepwise as the detachment proceeds.

© 2022 The Japan Society of Plasma Science and Nuclear Fusion Research

Keywords: plasma spectroscopy, extreme ultraviolet, vacuum ultraviolet, magnetically confined fusion, impurity seeding, resonant magnetic perturbation, divertor detachment

DOI: 10.1585/pfr.17.2402022

1. Introduction

Reduction of the divertor heat load is one of the most important issues for ITER and future fusion reactors [1, 2]. To reduce the divertor heat load, it is being studied in various devices to increase the radiation loss of impurities in the edge and divertor region, which is the so-called "divertor detachment" or radiative divertor operation. In the Large Helical Device (LHD), several operation scenarios have been proposed and applied to realize and maintain the divertor detachment. One of the methods to induce the divertor detachment is impurity seeding, where gas-puffing of nitrogen or noble gases are frequently used [3–8]. When impurities are introduced in the plasma, they are ionized and then some of them are distributed in the edge plasma

with lower ionization states, while others are distributed in the core plasma with higher ionization states. Impurity ions in the edge plasmas may contribute to maintaining the divertor detachment by acting as a radiation source, while impurity ions in the core plasmas may cause plasma dilution and lead to deterioration of plasma confinement. Therefore, it is important to monitor both edge impurities in low charge states and core impurities in high charge states simultaneously, in order to establish both an effective divertor detachment and good core confinement. The other method is application of resonant magnetic perturbation (RMP) [9–14]. In LHD, a magnetic island with the poloidal mode number, m , and the toroidal mode number, n , of $m/n = 1/1$ can be formed by RMP at the edge stochastic layer. It has been reported that the impurity emission was enhanced around the edge island created by RMP, which is a favorable effect on the formation of the

author's e-mail: oishi@nifs.ac.jp

^{*)} This article is based on the presentation at the 30th International Toki Conference on Plasma and Fusion Research (ITC30).

detached divertor from the viewpoint that it promotes impurity radiation in the plasma edge [12]. Based on the experience of these divertor detachment experiments accumulated in LHD, this study attempts to form and maintain a stable divertor detachment by Ne seeding and RMP application in electron cyclotron resonance (ECR)-heated discharges, aiming at compatibility of high electron temperature and low divertor heat load. In order to discuss how the impurity ions behave in the formation of divertor detachment, the spatial profiles of emission from Ne ions in multiple charge states are measured via space-resolved spectroscopy.

2. Experimental Setup

LHD is a heliotron type plasma confinement device which has major/minor radii of 3.6/0.64 m in the standard magnetic configuration with a maximum plasma volume of 30 m³ and a toroidal magnetic field of 3 T [15]. The coil system consists of a set of two continuous superconducting helical coils with a poloidal pitch number of 2 and a toroidal pitch number of 10, and also three pairs of superconducting poloidal coils.

A horizontally-elongated poloidal cross section of the LHD plasma and observation geometry of two space-resolved flat-field grazing incidence extreme ultraviolet (EUV) spectrometers, which are named “EUV Short2” [16] and “EUV Long2” [17–19], are illustrated in Fig. 1. LHD has ten toroidal sections, and the spectrometers are installed at a port called 10-O, which is on the outboard side of the 10th toroidal section. A gold-coated concave varied-line-spacing (VLS) laminar-type holographic grating with a groove density of 2400 grooves/mm and 1200 grooves/mm is mounted in EUV Short2 and EUV Long2, respectively. The observable wavelength range of EUV Short2 can be set within a range of 5 - 130 Å. In this study, the wavelength range is set to 8.5 - 18 Å to observe the line spectra of NeIX 13.5 Å and NeX 12.1 Å simultaneously. The observable wavelength range of EUV Long2 can be set within a range of 30 - 650 Å. In this study, the wavelength range is set to 98 - 137 Å to observe the line spectra of NeVI 123 Å, NeVII 106 Å, and NeVIII 103 Å simultaneously. EUV Short2 and EUV Long2 have a spatial resolution in the vertical direction by mounting a space-resolved slit at the position of the entrance slit. A CCD detector (1024 × 255 pixels, pixel size 26 × 26 μm², Andor DO920P-BN) is placed at the position of the exit slit of each spectrometer. The long axis of the detector plane is directed perpendicular to the midplane of the LHD plasma and the spatial observation range is set to project the emission profile of the upper half of the plasma at the horizontally-elongated poloidal cross section on the detector. Five-pixel binning is applied to the long axis of the detector with 1024 pixels. Thus, the observation range is resolved by 204 viewing chords in the vertical direction. The observation range covers approximately 500 mm in

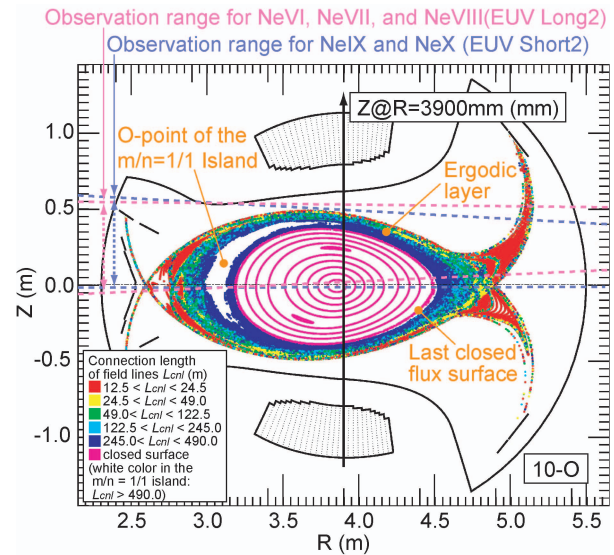


Fig. 1 Horizontally-elongated poloidal cross section of the LHD plasma and observation geometry of EUV Short2 and EUV Long2.

the vertical direction with a spatial resolution of 2.6 mm around the plasma center, as illustrated in Fig. 1. The short axis of the detector is directed to the wavelength dispersion direction and two-pixel binning is applied. The temporal resolution is 100 ms, which consists of approximately 60 ms exposure time and 40 ms reading time, under the operational conditions employed in this study.

The magnetic island is formed by RMP in such a way that the O-point is located on the outboard side at the 6th section (so-called “6-O island”), which is separated by 144 degrees counterclockwise in the toroidal direction from the 10-O port. In this study, we use a magnetic field configuration with a magnetic axis position, R_{ax} , of 3.85 m so that the magnetic island with $m/n = 1/1$ is located in the ergodic layer, which is a statistical magnetic field region in the plasma edge outside the last close flux surface (LCFS). The toroidal field strength, B_t , is 2.665 T and is directed counterclockwise when viewed from above. A Poincaré plot of the magnetic field lines of this magnetic field configuration with the 6-O magnetic island in the 10-O toroidal section is shown in Fig. 1. The connection length of field lines, L_{cni} , is color-coded according to the length range. The white area inside the $m/n = 1/1$ magnetic island has a connection length longer than 490 m. Since the magnetic island has a spatial structure of $m/n = 1/1$, the island O-point is located on the inboard side of the upper half of the plasma in the 10-O toroidal section.

3. Temporal Evolution of NeIII-NeX Emission Line Intensities

Figure 2 shows a waveform of an ECR-heated discharge with divertor detachment by RMP application and Ne gas injection in LHD. In this figure, temporal evolu-

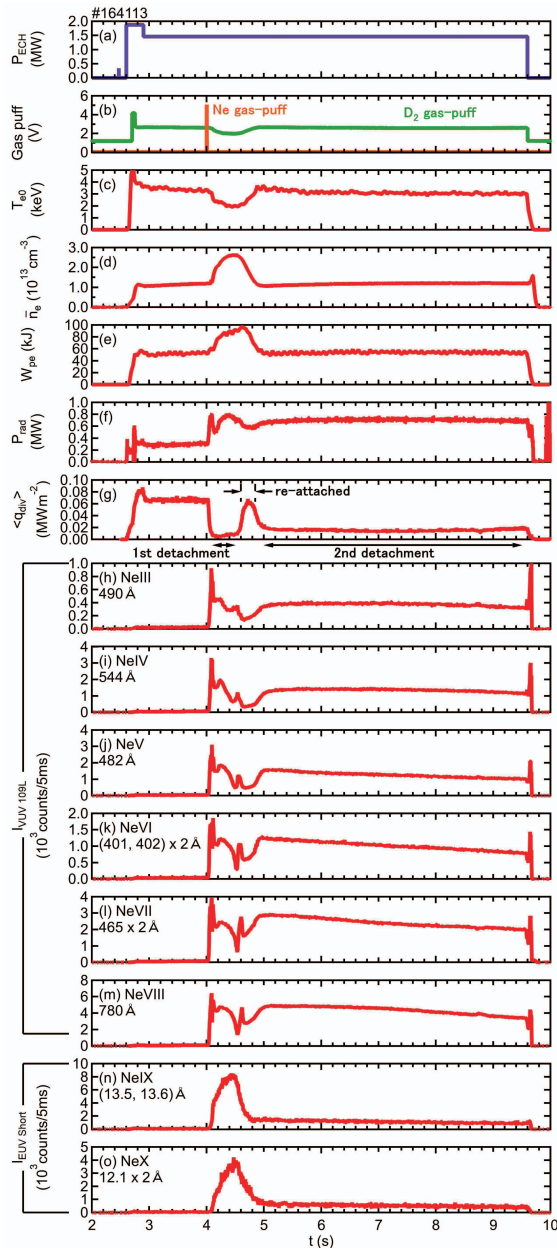


Fig. 2 Waveform of an ECR-heated discharge with divertor detachment by RMP application and Ne gas injection in LHD: (a) heating power of ECH, (b) gas-puffing duration of Ne and D₂, (c) central electron temperature, T_{e0} , (d) line-averaged electron density, \bar{n}_e , (e) electron kinetic energy, W_{pe} , (f) total radiation power, P_{rad} , and (g) toloidally-averaged divertor heat flux, $\langle q_{div} \rangle$. Temporal evolutions of Ne line intensities plotted together for (h) NeIII (488.11, 488.88, 489.50, 489.65, 490.31, 491.05) Å, (i) NeIV (541.13, 542.07, 543.88) Å, (j) NeV (481.29, 481.37, 482.99) Å, (k) NeVI (401.15, 401.94) × 2 Å, (l) NeVII 465.22 × 2 Å, (m) NeVIII 780.32 Å, (n) NeIX (13.45, 13.55) Å, and (o) NeX (12.13, 12.14) × 2 Å.

tion of (a) heating power of the electron cyclotron heating (ECH), (b) gas-puffing waveforms of Ne and D₂, (c) central electron temperature, T_{e0} , (d) line-averaged electron density, \bar{n}_e , (e) electron kinetic energy, W_{pe} , (f) total radiation power, P_{rad} , and (g) toloidally-averaged divertor

heat flux, $\langle q_{div} \rangle$ are plotted together. $\langle q_{div} \rangle$ is measured by the Langmuir probes mounted on the divertor plates at the inboard side of the torus, and it is employed as an indicator of the divertor heat load [5]. The plasma was initiated and heated by ECH using 77 GHz and 154 GHz gyrotrons with the electron cyclotron resonance at a magnetic field strength of 2.75 T. The power-deposition profile of ECH, calculated by a ray-tracing code integrated with 3D equilibrium mapping “LHDGauss” [20], had a peak around $r_{eff}/a_{99} = 0.3$, where r_{eff} is the effective minor radius and a_{99} is the plasma edge defined as the effective minor radius in which 99% of electron stored energy is enclosed [21]. D₂ gas was puffed from 2.7 to 9.6 s for the particle fueling. The D₂ gas-puffing rate was feedback-controlled to maintain the electron density at $1 \times 10^{13} \text{ cm}^{-3}$. Reduction of the divertor heat load was aimed by Ne seeding at 4.000 to 4.005 s for triggering the divertor detachment. After the Ne gas puffing, T_{e0} decreased and \bar{n}_e , W_{pe} , and P_{rad} increased rapidly. In this paper, the divertor detachment is defined by reduction of this $\langle q_{div} \rangle$ value. The $\langle q_{div} \rangle$ value decreased suddenly at 4.03 s and the reduced heat flux was sustained from 4.1 to 4.5 s. In this time period, $\langle q_{div} \rangle$ was reduced down to about 10% compared to the heat flux level before Ne puffing, which is denoted as the “1st detachment” phase in Fig. 2 (g). Then $\langle q_{div} \rangle$ recovered from 4.5 s together with an increase of T_{e0} and decreases of \bar{n}_e and W_{pe} . In a short time period from 4.6 to 4.8 s, $\langle q_{div} \rangle$ returned to the level before the Ne puff, which is denoted as the “re-attached” phase in Fig. 2 (g). After the re-attached phase, $\langle q_{div} \rangle$ was reduced again down to about 30% compared to the heat flux level before Ne puffing, which is denoted as the “2nd detachment” phase in Fig. 2 (g). The 2nd detachment was maintained by the end of the discharge. Thus, it turned out that there were two divertor detachment phases in this discharge. It should be noted for future discussion that there is a concern whether the heat flux at the inboard side of the torus is representative of the heat flux in the entire poloidal direction because the helical devices are asymmetric in the poloidal direction. Recently, the analysis of the probe signals installed at the lower part of the torus was started, and as a result, the reduction of the heat flux was observed even in the lower part of the torus as in the inboard part of the torus. In the future, the results observed at several poloidal locations will be compared with EMC3-EIRENE simulations to improve the accuracy of the theoretical model, and then the discussion will be extended to the prediction of the three-dimensionality of the divertor detachment. However, at present, the heat flux measured at the inboard side of the torus is used for the discussion of the divertor detachment.

We have already observed the wavelength spectra including line emissions of NeIII–NeX simultaneously in the Ne seeded divertor heat load reduction experiment at LHD using EUV and vacuum ultraviolet (VUV) spectroscopic diagnostics; and the wavelengths of useful emission lines for the spectroscopic studies were summarized [22]. Figure 2 also shows temporal evolutions of Ne line intensi-

ties for (h) NeIII (488.11, 488.88, 489.50, 489.65, 490.31, 491.05) Å, (i) NeIV (541.13, 542.07, 543.88) Å, (j) NeV (481.29, 481.37, 482.99) Å, (k) NeVI (401.15, 401.94) Å (second order), (l) NeVII 465.22 Å (second order), (m) NeVIII 780.32 Å, (n) NeIX (13.45, 13.55) Å, and (o) NeX (12.13, 12.14) Å (second order). A normal incidence 20 cm VUV spectrometer “VUV 109L” [23] was used for the observation of NeIII-NeVIII lines and a grazing incidence flat-field EUV spectrometer “EUV Short” [24] was used for the observation of NeIX and NeX lines. Identification of Ne line emissions was conducted based on the wavelength database of NIST [25] for NeIII-NeIX lines as well as Ref. [26] for NeX lines. In the 1st detachment phase, intensities of all of NeIII-NeX lines increased. And then they decreased in the re-attached phase. In the 2nd detachment phase, NeIII-NeVIII lines increased again up to large emission intensity levels comparable to those in the 1st detachment phase, while NeIX and NeX lines further decreased and kept small emission intensity levels by the end of the discharge. This observation suggests that the two detachment phases have different characteristics of impurity emission. Therefore, a more detailed comparison of the spatial profiles of impurity emissions between the two detachment phases was attempted via space-resolved EUV spectroscopy, as stated in the next section.

4. Spatial Profiles of NeVI-NeX Emission Lines

Simultaneous measurement of the spatial profiles of NeVI-NeX has succeeded via the space-resolved EUV spectroscopy. Since the ionization potentials of NeVI-NeX are different (ionization potential = 158 eV, 207 eV, 239 eV, 1196 eV, and 1362 eV for NeVI, NeVII, NeVIII, NeIX, and

NeX, respectively), their distributed locations are also different. Therefore, this measurement enables us to discuss the Ne ion profiles from the core to the edge comprehensively. Figure 3 shows two-dimensional CCD images obtained via the space-resolved EUV spectroscopy in the 2nd detachment phase of the identical discharge, as shown in Fig. 2. The horizontal axes of the images are vertical locations of the observation chords at the major radius of 3900 mm, $Z_{R=3900\text{mm}}$. Right and left-hand sides of the axes correspond to the observation chords located close to the midplane and close to the top edge of the plasma, respectively. The vertical axes are wavelength and white brightness is the intensity of each emission line. As results, NeIX and NeX lines were observed by EUV Short2, as shown in Fig. 3 (a) and NeVI-NeVIII lines were observed by EUV Long2, as shown in Fig. 3 (b). The spatial profile of the emission line intensity is obtained by extracting the wavelength region containing the target emission line from these two-dimensional data.

Figure 4 shows spatial profiles of T_e , n_e , and NeVI-NeX emission intensity in the time period from just before Ne gas-puffing to the 1st detachment phase. Radial profiles of (a) T_e and (b) n_e are plotted against the major radius on the midplane of a horizontally-elongated cross section, which is the actual coordinate of the Thomson scattering measurement point. The T_e and n_e profiles from around the magnetic axis to the outboard side at the cross section are displayed. Vertical profiles of emission intensities of (c) NeVI 123 Å, (d) NeVII 106 Å, and (e) NeVIII 103 Å measured using EUV Long2 and (f) NeIX 13.5 Å and (g) NeX 12.1 Å measured using EUV Short2 are shown together. The position of the LCFS in the vacuum magnetic field is also indicated. In this time period, T_e decreased while n_e increased at the onset of the 1st detachment. It

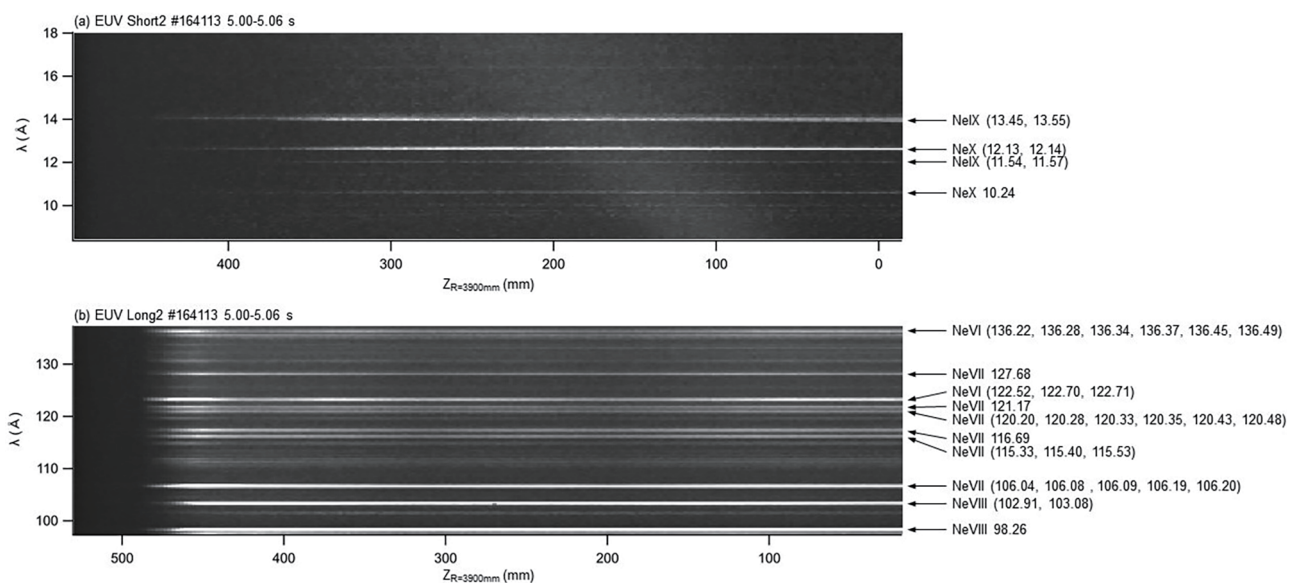


Fig. 3 Two-dimensional CCD images obtained from an ECR-heated discharge with divertor detachment by RMP application and Ne gas injection using (a) EUV Short2 and (b) EUV Long2.

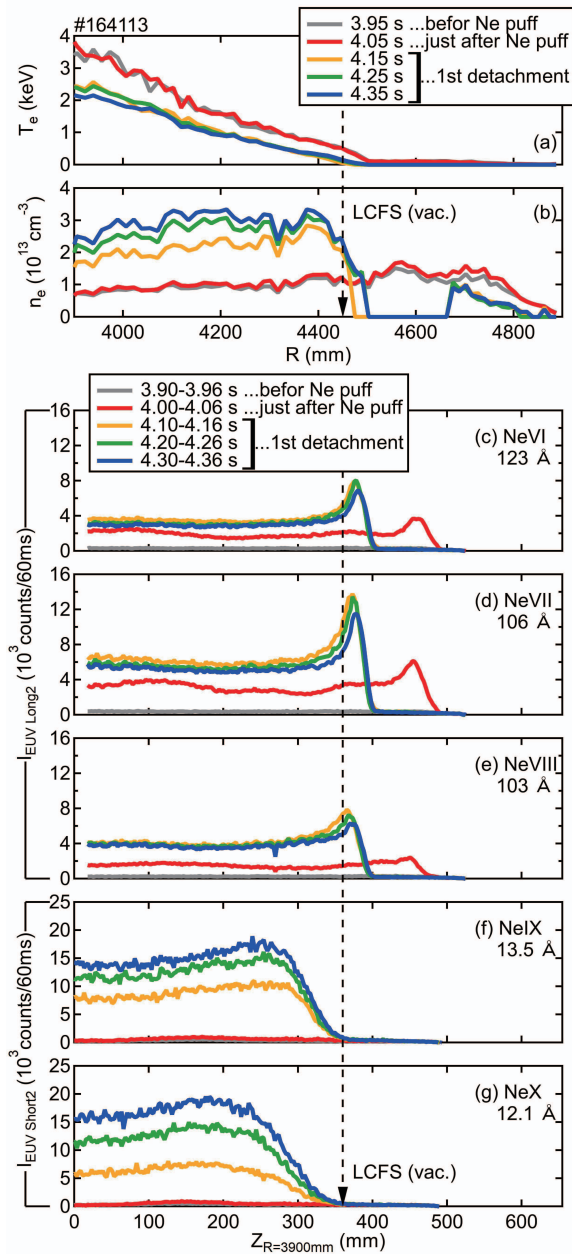


Fig. 4 Spatial profiles of T_e , n_e , and NeVI-NeX emission intensity in the time period from just before Ne gas-puffing to the 1st detachment phase. Radial profiles of (a) T_e and (b) n_e plotted against the major radius on the midplane of a horizontally-elongated cross section. Vertical intensity profiles of (c) NeVI 123 Å, (d) NeVII 106 Å, and (e) NeVIII 103 Å measured using EUV Long2 and (f) NeIX 13.5 Å and (g) NeX 12.1 Å measured using EUV Short2. The position of LCFS in the vacuum magnetic field also indicated.

is also worth mentioning an interesting observation that the electron density became almost zero in the region of $R = 4500 - 4650$ mm when the 1st detachment occurred. This suggests that the plasma was distributed in the ergodic layer outside the LCFS before the 1st detachment, and the practical boundary of the plasma confinement region shrank radially to around the LCFS when the 1st detachment

occurred. Spatial profiles of NeVI-NeVIII had a peak far outside the LCFS ($Z = 460$ mm) before the 1st detachment. Since NeVI-NeVIII are reasonably distributed in the ergodic layer, considering the ionization potential, the observed emission intensity becomes larger with a longer integral length of the observation chord through the ergodic layer, resulting in a spatial profile with a peak at the edge. When the 1st detachment occurred, the peak moved to the position near the LCFS ($Z = 380$ mm) accompanied by an increase of the emission intensity, while emission intensity of NeIX and NeX increased within the LCFS. These observations suggest that Ne ions were penetrated inside the LCFS and acted as a radiation source in the 1st detachment phase. Although the divertor heat load was well reduced, T_e of the core plasmas also decreased.

Figure 5 shows spatial profiles of T_e , n_e , and NeVI-NeX emission intensity in the time period from the 1st detachment phase to the re-attached phase. T_e increased and n_e decreased, both changing to be closer to the states before Ne gas-puffing. The n_e profile returned to the state where it was also distributed in the ergodic layer outside the LCFS. The emission location of NeVI-NeVIII moved from near the LCFS ($Z = 380$ mm) to far outside the LCFS ($Z = 460$ mm). The emission intensity of NeIX and NeX gradually decreased within the LCFS. It is noted that the lower charge state emission profile (NeVI-NeVIII) shows a stepwise shift in radial direction, that is, the outermost peaks are located either at $Z = 460$ or 380 mm, with no stable emission in-between. The results indicate that the edge island structure affects the stability of impurity emission distribution.

Figure 6 shows spatial profiles of T_e , n_e , and NeVI-NeX emission intensity in the time period from the re-attached phase to the 2nd detachment phase. Both T_e and n_e returned to the profiles before Ne gas-puffing. The emission intensity of NeVI-NeVIII increased outside the LCFS ($Z = 360 - 460$ mm) while the emission intensity of NeIX and NeX was kept at a low level within the LCFS. These observations suggest that Ne ions as the radiation source in the 2nd detachment phase was localized outside the LCFS and penetration of Ne ions inside the LCFS was not so significant. Thus, low divertor heat load and high T_e were obtained simultaneously.

An interesting feature of the NeVI-NeVIII emission intensity profiles in the 2nd detachment is that small peaks with different locations appear for each charge state in addition to the large peak outside the LCFS. Figure 7 shows the relationship between peak positions of the NeVI-NeVIII emission intensity profiles and the spatial structure of the magnetic field, including the shape of the $m/n = 1/1$ island formed by RMP. Large peaks located outside the LCFS, such as $Z = 455$ mm for NeVI, $Z = 445$ mm for NeVII, and $Z = 420$ mm for NeVIII, correspond to the emission from Ne ions distributed in the edge ergodic layer. Moreover, several small peaks were observed only in the 2nd detachment phase, such as $Z = 90$ mm and 250 mm

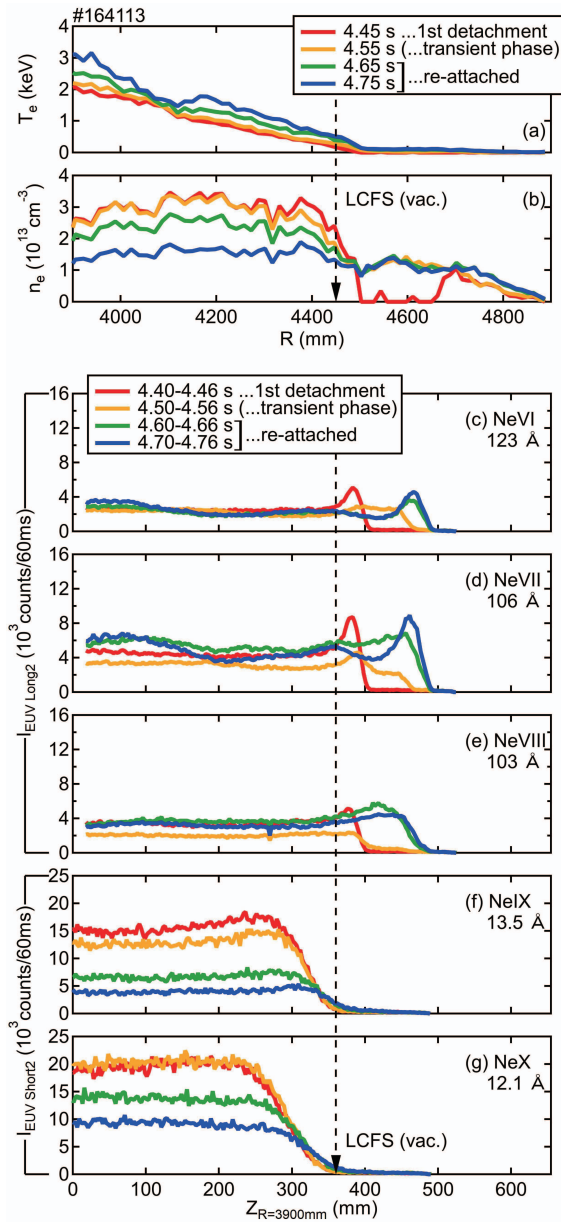


Fig. 5 Spatial profiles of T_e , n_e , and NeVI-NeX emission intensity in the time period from the 1st detachment phase to the re-attached phase. Radial profiles of (a) T_e and (b) n_e plotted against the major radius on the midplane of a horizontally-elongated cross section. Vertical intensity profiles of (c) NeVI 123 Å, (d) NeVII 106 Å, and (e) NeVIII 103 Å measured using EUV Long2 and (f) NeIX 13.5 Å and (g) NeX 12.1 Å measured using EUV Short2.

for NeVI, $Z = 130$ mm and 230 mm for NeVII, and $Z = 150$ mm for NeVIII. Observation chords which correspond to the locations of the emission intensity peaks are illustrated in Fig. 7 (a). It is seen that the modulation in the Z direction is most pronounced in the lower charge state emission, NeVI (ionization potential = 158 eV), and the profile becomes smoother toward the higher charge state emission, NeVIII (ionization potential = 239 eV). Provided that the emission profile is strongly affected by the magnetic field structure, the results suggest that there is a transition

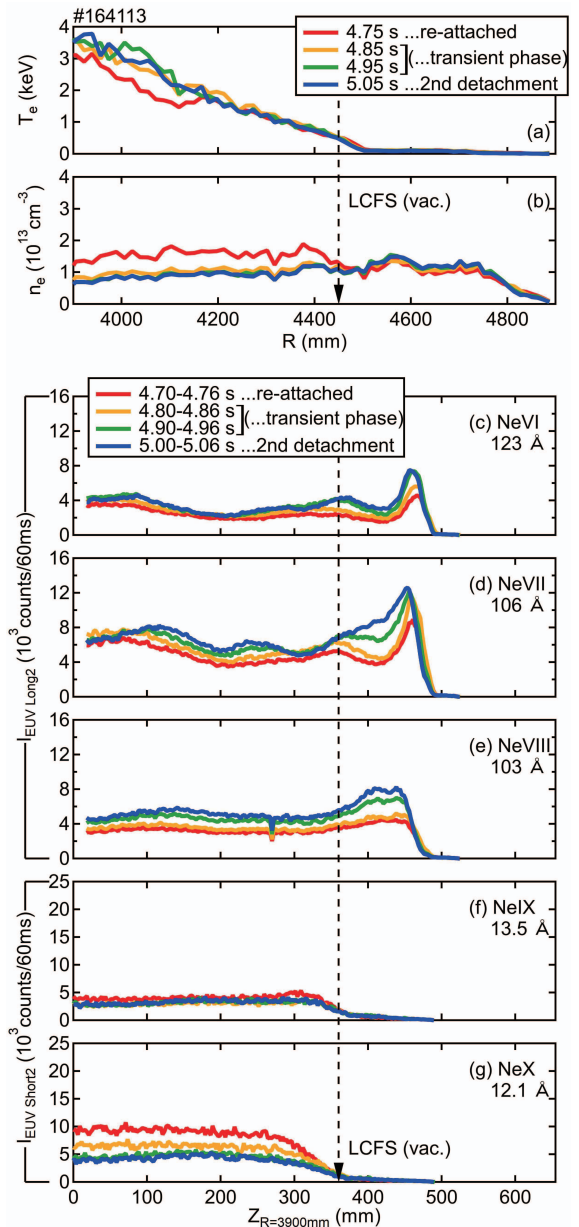


Fig. 6 Spatial profiles of T_e , n_e , and NeVI-NeX emission intensity in the time period from the re-attached phase to the 2nd detachment phase. Radial profiles of (a) T_e and (b) n_e plotted against the major radius on the midplane of a horizontally-elongated cross section. Vertical profiles of emission intensities of (c) NeVI 123 Å, (d) NeVII 106 Å, and (e) NeVIII 103 Å measured using EUV Long2 and (f) NeIX 13.5 Å and (g) NeX 12.1 Å measured using EUV Short2.

of the magnetic field structure at the radial range where these emissions are situated. In order to further investigate the relationship between the position of the emission and the magnetic island structure, it would be useful to compare the spectroscopic observations with two-dimensional measurements such as imaging bolometers [27] as well as three-dimensional simulations such as EMC3-EIRENE [28], and is a subject for future work.

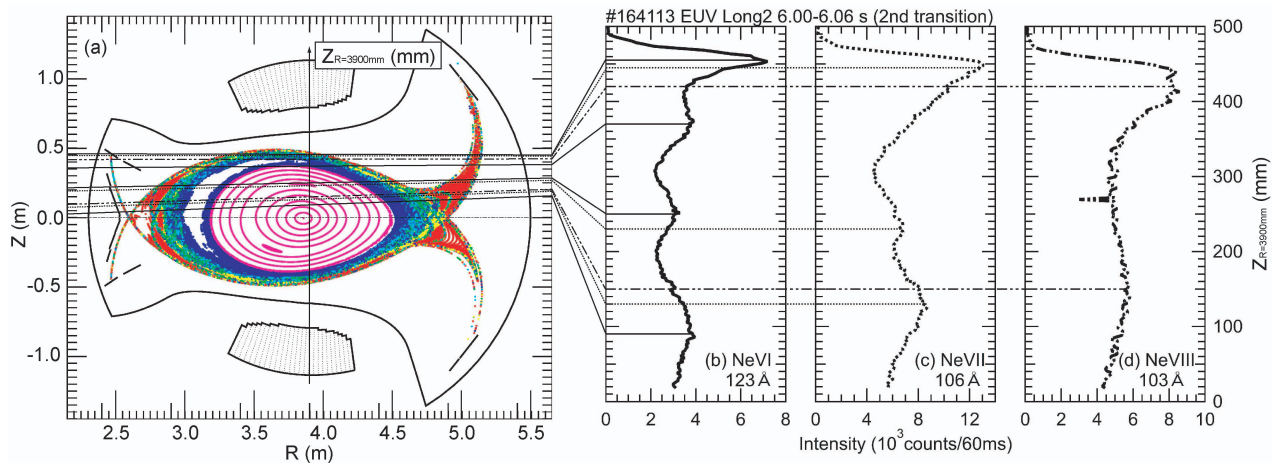


Fig. 7 (a) Poloidal cross section of the plasma in the 10-O toroidal section observed by EUV Long2 and the vertical profiles of emission intensities of (b) NeVI 123 Å, (c) NeVII 106 Å, and (d) NeVIII 103 Å measured using the EUV Long2 in the 2nd detachment phase. Observation chords which correspond to the locations of the emission intensity peaks illustrated in (a).

5. Summary

Induction of the divertor detachment has been attempted in LHD by application of RMP and Ne gas puffing in ECR-heated discharges for compatibility of high central electron temperature and low divertor heat load. Two kinds of divertor detachment phases were observed. The 1st detachment phase appeared transiently just after the Ne gas puffing, and the 2nd detachment phase appeared steadily in the latter half of the discharge. Space-resolved EUV spectroscopy revealed that the spatial profile of the Ne emission intensity varied as follows, when the divertor detachment occurred. In the 1st detachment phase, NeVI-NeVIII emissions increased slightly outside the LCFS, while NeIX and NeX emissions increased inside the LCFS. Although in the 1st detachment the divertor heat load was significantly reduced, the central electron temperature also decreased because the Ne ions were penetrated inside the LCFS as a radiation source. In the 2nd detachment phase, NeVI-NeVIII emissions increased outside the LCFS while NeIX and NeX emissions kept low intensity inside the LCFS. In this phase, low divertor heat load and high central electron temperature were obtained simultaneously because the Ne ions were localized outside the LCFS as radiation source. The profile measurements of NeVI-NeVIII emission have revealed a significant impact of edge magnetic field structure induced by the RMP application, such as the magnetic island, on the impurity emission distribution, which shows stepwise radial shifts depending on radiation level. Other discharges with different conditions, such as electron density, species of injected gas and heating power, will be analyzed in the future to integrate knowledge and experience on the stable sustainment of the divertor detachment.

Acknowledgments

The authors thank all the members of the LHD team for their cooperation with the LHD operation. This work

is partially supported by JSPS KAKENHI Grant Numbers JP20K03896 and JP19H01878.

- [1] ITER Physics Basis, “Chapter 4: Power and particle control”, Nucl. Fusion **39**, 2391 (1999).
- [2] M. Shimada *et al.*, Nucl. Fusion **47**, S1 (2007).
- [3] S. Masuzaki *et al.*, J. Nucl. Mater. **438**, S133 (2013).
- [4] K. Mukai *et al.*, Nucl. Fusion **55**, 083016 (2015).
- [5] H. Tanaka *et al.*, Nucl. Mater. Energy **12**, 241 (2017).
- [6] C. Suzuki *et al.*, Nucl. Mater. Energy **14**, 195 (2019).
- [7] K. Mukai *et al.*, Plasma Fusion Res. **15**, 1402051 (2020).
- [8] K. Mukai *et al.*, Nucl. Fusion **61**, 126018 (2021).
- [9] M. Kobayashi *et al.*, Phys. Plasmas **17**, 056111 (2010).
- [10] M. Kobayashi *et al.*, Nucl. Fusion **53**, 093032 (2013).
- [11] H.M. Zhang *et al.*, Plasma Fusion Res. **11**, 2402019 (2016).
- [12] H.M. Zhang *et al.*, Phys. Plasmas **24**, 022510 (2017).
- [13] M. Kobayashi *et al.*, Nucl. Fusion **59**, 096009 (2019).
- [14] M. Kobayashi and M.Z. Tokar, Contrib. Plasma Phys. **60**, e201900138 (2020).
- [15] Y. Takeiri *et al.*, Nucl. Fusion **57**, 102023 (2017).
- [16] X.L. Huang *et al.*, Rev. Sci. Instrum. **85**, 043511 (2014).
- [17] C.F. Dong *et al.*, Rev. Sci. Instrum. **81**, 033107 (2010).
- [18] E.H. Wang *et al.*, Rev. Sci. Instrum. **83**, 043503 (2012).
- [19] H.M. Zhang *et al.*, Jpn. J. Appl. Phys. **54**, 086101 (2015).
- [20] T. Ii Tsujimura *et al.*, Nucl. Fusion **55**, 123019 (2015).
- [21] K.Y. Watanabe *et al.*, Plasma Phys. Control. Fusion **49**, 605 (2007).
- [22] T. Oishi *et al.*, Plasma Fusion Res. **16**, 2402006 (2021).
- [23] T. Oishi *et al.*, Plasma Fusion Res. **10**, 3402031 (2015).
- [24] M.B. Chowdhuri *et al.*, Appl. Opt. **47**, 135 (2008).
- [25] A. Kramida *et al.*, (2021). NIST Atomic Spectra Database (ver. 5.9), [Online]. Available: <https://physics.nist.gov/asd> [2021, November 26]. National Institute of Standards and Technology, Gaithersburg, MD. DOI: <https://doi.org/10.18434/T4W30F>
- [26] R.L. Kelly, J. Phys. Chem. Ref. Data **16**, Suppl. 1 (1987).
- [27] B.J. Peterson *et al.*, Nucl. Mater. Energy **26**, 100848 (2021).
- [28] G. Kawamura *et al.*, Plasma Phys. Control. Fusion **60**, 084005 (2018).